Vacuum Deposited 2D/3D Perovskite Heterojunctions

Maria-Grazia La-Placa[†], *Lidón Gil-Escrig*[‡], *Dengyang Guo*[‖], *Francisco Palazon*[†], *Tom J. Savenije*[‖], *Michele Sessolo*[†],* *Henk J. Bolink* [†]

[†] Instituto de Ciencia Molecular, Universidad de Valencia, C/ Beltrán 2, Paterna, 46980, Spain

[‡] Helmholtz-Zentrum Berlin für Materialien und Energie GmbH, Young Investigator Group for Perovskite Tandem Solar Cells, Kekuléstraße 5, Berlin, 12489, Germany

[‖] Department of Chemical Engineering, Delft University of Technology, Delft, 2629 HZ, The Netherlands

Corresponding Author: michele.sessolo@uv.es

Abstract. Low-dimensional (quasi-) 2D perovskites are being extensively studied in order to enhance the stability and the open-circuit voltage of perovskite solar cells. Up to no, thin 2D perovskite layers on the surface and/or at the grain boundaries of 3D perovskite have been deposited solely by solution processing, leading to unavoidable intermixing between the two phases. In this work, we report the fabrication of 2D/3D/2D perovskite heterostructures by dual source vacuum deposition, with the aim of studying the interaction between the 3D and 2D phases as well as the charge transport properties of 2D perovskites in neat 2D/3D interfaces. Unlike what normally observed in solution-processed 3D/2D systems, we found a reduced charge transport with no direct evidence of surface passivation. This is likely due to a non-favorable orientation of the 2D perovskite with respect to the MAPI and to the formation of 2D phases with very low dimensionality (virtually pure 2D).

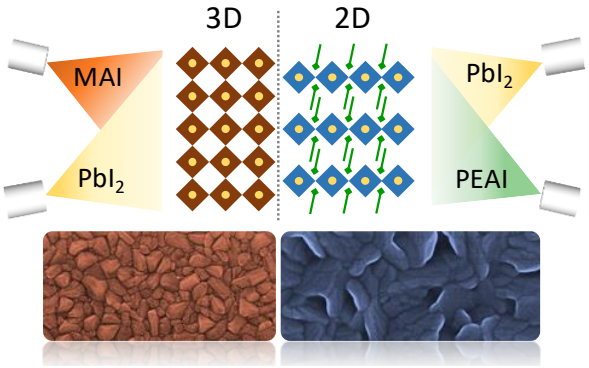

Organic–inorganic metal halide perovskites are being widely studied because of their exceptional optoelectronics properties, i.e. high absorption coefficient, ambipolar charge transport, easy-to-tune bandgap, among others.[1–3] Importantly, high quality perovskite films can be deposited through a variety of scalable methods, either from solution or in vacuum, and assembled into optoelectronic thin-film devices.[4,5] These properties lead to the demonstration of perovskite solar cells (PSCs) with certified power conversion efficiency (PCE) of 24% in only 10 years of development.[6] The most widely studied perovskite compositions, such as methylammonium lead iodide ($CH_3NH_3PbI_3$, MAPI), are based on the three-dimensional (3D) AMX_3 structure, where A represents a monovalent organic or inorganic cation, typically methylammonium (MA), formamidinium (FA), or caesium (Cs^+), M is a divalent metal cation (Pb^{2+} or Sn^{2+}) and X is a halide (Cl^-, Br^-, I^-). [7–10] In spite of the high efficiency PSCs demonstrated for these materials, polycrystalline perovskite thin films still contain defects, notably at the surface, which limits the device performance as a consequence of non-radiative charge recombination.[11,12] Defects on the surface and on the grain boundaries also play an important role in the permeation of moisture or oxygen into the perovskite film, accelerating the film/device degradation. Several methods have been reported to simultaneously passivate and enhance the stability of perovskites[13], most notably the use of additive, alternative precursors or altered stoichiometry,[14–16] embedding small alkali metal cations[17–19], or the use of thin organic buffer layers at the perovskite/transport material interface. [20–23]

More recently, several works reported on mixed dimensional perovskites, using monoammonium or diammonium cations which interact with the 3D perovskite, not only passivating surface defects but also improving the device stability, thanks to the hydrophobic character of the alkylammonium chains.[24,25] The structural analysis of modified 3D perovskite films suggested the coexistence of two distinct phases: a 3D perovskite layer and a 2D (layered) perovskite. 2D perovskites form when the inorganic lead halide framework cannot accommodate the large organic cations into a 3D structure, and collapses into a low dimensional material with inorganic sheets separated by the organic cations. The general formula for pure 2D perovskites is $(R\text{-}NH_3)_2MX_4$, where R is an aliphatic or aromatic group. The layered perovskite family is not restricted solely to this structure and thicker inorganic sheets can be incorporated as well. In the Ruddlesden–Popper layered perovskites with formula $(RNH_3)_2(A)_{n-1}Pb_nI_{3n+1}$ the thickness of the inorganic layers increases with increasing n.[26] The properties of this last class of materials, also known as quasi-2D perovskite, have been widely studied.[2728] It was shown that solar cells with $n < 40$ show inferior performance as a consequence of a reduced charge carrier mobility.[2930] Ruddlesden–Popper perovskites have been applied to light-emitting diodes and solar cells, showing good charge transport properties, enhanced photovoltage and stability.[29,31–37383940]

A complementary approach involves the use of 2D-3D bilayers. The underlying concept is to combine the high efficiency of 3D absorber with the stabilization and passivation properties of 2D perovskites.[41] These

bilayers can be prepared by functionalization of the 3D perovskite surface with large ammonium cations, resulting in the formation of a thin low dimensional perovskite layers.[42–454647,4849] Alternatively, the direct processing of a 2D perovskite film on top of a pre-formed 3D material can also be beneficial for the bottom perovskite film.[5051] Up to now the introduction of thin 2D perovskite layers on the surface and/or at the grain boundaries of 3D perovskite has been carried out solely by solution processing, leading to unavoidable intermixing between the 2D and 3D perovskites, with the formation of an intermediate, low dimensional quasi-2D layer.[52] Vacuum deposition is an alternative solvent-free technique suited to develop multilayer perovskite structures.[53] Vacuum processing of perovskites is intrinsically additive, eliminating issues such as the solubility limitation of precursors, or the need of orthogonal solvents in order to process multilayer devices.[54,55] At the same time, it allows a fine control over the film thickness and the deposition of high purity semiconductors.[56,57] Recently, a 3D/2D heterojunction produced exclusively by vacuum methods has been reported.[58] The heterojunction consisted in a MAPI film (formed by conversion of a sublimed PbI_2 layer converted with MAI vapors), subsequently exposed to butylammonium iodide vapors, forming a surface layer of the quasi-2D perovskite $(BA)_2(MA)_{n-1}Pb_nI_{3n+1}$, with $n \approx 3$. While an increase in stability was found for the surface-modified solar cells, the performance and especially the photovoltage was not found to improve as compared to the reference MAPI devices.

In this work, we report the fabrication of 2D/3D perovskite heterojunctions by dual source vacuum deposition, with the aim of studying the interaction between the 3D and 2D phases as well as the charge transport properties of 2D perovskites in neat 2D/3D interfaces. We prepared 2D/MAPI/2D perovskite heterostructures by employing pure MAPI (3D) and pure phenethylammonium lead iodide (PEA_2PbI_4, 2D). These structures where integrated in vacuum deposited perovskite solar cells. In order to rationalize the role of each interface, we also separately studied the two possible bilayer configurations, 2D/MAPI and MAPI/2D. Unlike what observed in solution-processed 3D/2D films, we observed a generally hindered charge transport with no direct evidence of surface passivation. These phenomena are likely due to a non-favorable orientation of the 2D perovskite with respect to the MAPI (growth parallel to the substrate and impeding charge transport) and to the formation of 2D phases with very low dimensionality (n virtually equal to 1). In spite of to the lower mobility and unfavorable orientation of the 2D perovskite, we identified a tradeoff between the open circuit voltage (V_{oc}, which was found to increase up to 1.1 V) and fill factor (FF, related to charge transport), as a function of the 2D layer thickness.

The 2D-PEA_2PbI_4 perovskite thin films were prepared by co-sublimation of the precursor compounds, phenethylammonium iodide (PEAI) and lead iodide, upon calibration of the deposition rate for each material. The calibration factor was obtained by comparing the thickness of the thin-film detected from the quartz crystal microbalance sensors with that measured with a mechanical profilometer. PEAI can be sublimed with a stable and controlled deposition rate, however, it must be properly outgassed in high

vacuum before deposition. Details of the thin-film and device fabrication are provided in the Supporting Information. Estimation of layered PEA_2PbI_4 perovskite stoichiometry was performed off-line with X-ray diffraction (XRD). The diffractograms (**Figure 1**a) were collected for both pristine sample and for low-temperature annealed films (5 minutes at 100 °C in inert atmosphere). The as-prepared materials already show the expected XRD pattern for a 2D perovskite, meaning that crystallization occurs already at room temperature, as for vacuum deposited MAPI films.

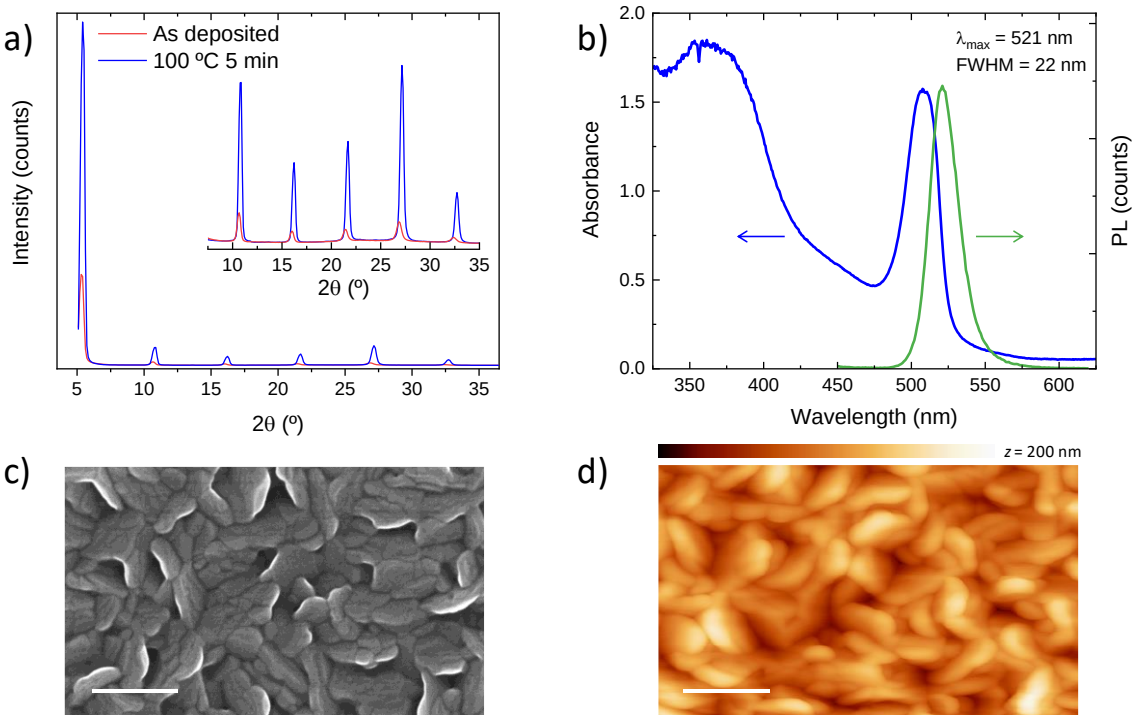

Figure 1. a) XRD patterns of 200 nm thick, vacuum deposited PEA_2PbI_4 perovskite thin films. b) Optical absorption and photoluminescence spectra (excitation at 375 nm), c) SEM image and d) AFM topography of PEA_2PbI_4 thin films after annealing at 100 ºC for 5 minutes. The scale bar in both microscopy images is 400 nm.

However, after the short low-temperature annealing, we observed more intense diffraction peaks, indicating a well-crystallized perovskite. The *c*-axis diffraction signals strongly dominate the diffraction pattern, with six observed [00l] peaks (5.4°, 10.8°, 16.3°, 21.7°, 27.2°, 32.8°) corresponding to the (002), (004), (006), (008), (0010), and (0012) crystal planes, respectively. The preferential orientation along the [00l] direction suggests that the 2D perovskite film grows with the alternating organic and inorganic sheets parallel to the substrate's plane. Such orientation is not a priori favorable for device operation, as the insulating organic

sheets would be perpendicular to the direction of charge transport. The optical absorption spectrum of the PEA_2PbI_4 films (Figure 1b) exhibit the characteristic components of 2D perovskites: a band in the UV-blue range, corresponding to the interband transitions leading to free carrier generation, and a red-shifted, intense peak at 508 nm, due to exciton absorption.[59] The corresponding photoluminescence (measured upon excitation with a continuous wave laser at 375 nm) shows the expected sharp emission peak with very small Stokes shift at 521 nm, with a full width at half-maximum of only 22 nm. Taken together, the XRD and the optical characteristics indicates the formation of a pure 2D (n =1) perovskite compound. The morphology of the layers was studied by scanning electron microscopy (SEM, Figure 1c) and atomic force microscopy (AFM, Figure 1d). The SEM shows a distinct morphology with well-defined, randomly distributed platelets (size up to 500 nm) composed by grains in the <100 nm range. These vacuum deposited 2D materials were found to be very reproducible and could maintain stable structural properties for more than 6 months (Figure S1).

We then used these 2D films to fabricate perovskite heterostructures. Initially, we deposited 10 nm thick PEA_2PbI_4 films below and on top of a 500 nm thick MAPI film, in order to investigate the influence of the 2D layers on the morphology and crystallinity of the 3D perovskite. The XRD patterns of a 3D sample on glass and sandwiched between 2D layers are presented in Figure S2. As can be observed for the reference sample (MAPI on glass), a preferential orientation occurs along the [ll0] direction, as commonly observed both for solution-processed and vacuum-deposited MAPI.[6061] However, when the MAPI layer is sandwiched between two PEA_2PbI_4 films, we observed a decrease in the intensity of the (110) and (220) peaks along with an increase of the (022) and (134) reflections. These observations suggest a change in the orientation of the MAPI film when deposited between 2D perovskites. The change of the diffraction profiles together with their enlarged FWHM also indicate a reduction of the crystals size for the MAPI film. We also noted a weak diffraction signal at low angle ($2\theta = 12.7^{o}$), ascribed to the presence of unreacted PbI_2, both in the pure MAPI and in the 2D/MAPI/2D heterostructure. The role of a small PbI_2 excess in MAPI films has been widely studied, but its effect has not been fully rationalized yet. Specifically, in vacuum deposited MAPI films and solar cells, the presence of resilient PbI_2 has been often identified and it seems not to interfere with charge generation and transport.[62,63] Interestingly, in several solution-processed 3D/2D perovskite systems, an excess PbI_2 is intentionally used as a platform to then form a low dimensional perovskite by simply spin-coating the corresponding organic ammonium halide.[41] In our case, the excess PbI_2 in the MAPI film is maintained even after deposition of the 2D PEA_2PbI_4 film. Considering that no PbI_2 diffraction could be observed in pure PEA_2PbI_4 films (meaning that the PbI_2 signal comes only from the underlying MAPI layer), these observations suggest that virtually no intermixing takes place between the two materials, resulting in a neat 3D/2D perovskite interface. The formation of a pure PEA_2PbI_4 film at

the interface with MAPI is also supported by the PL of a 2D/3D bilayer, where the signals corresponds to those of the pure separeted materials (Figure S7).

While no changes where observed in the optical absorption of the 2D/MAPI/2D heterostructures (Figure S3) as compared to the bare MAPI (the contribution of the very thin PEA_2PbI_4 films is not noticeable since the 3D absorption saturates in the green-blue region of the spectrum), we did observe differences in their morphology. The morphology of the 3D layer with and without the 2D perovskite interlayers was investigate by scanning electron microscopy (SEM). The surface of the MAPI film appears homogeneous and compact (**Figure 2**a), composed by grains with an average size of approximately 100 nm.

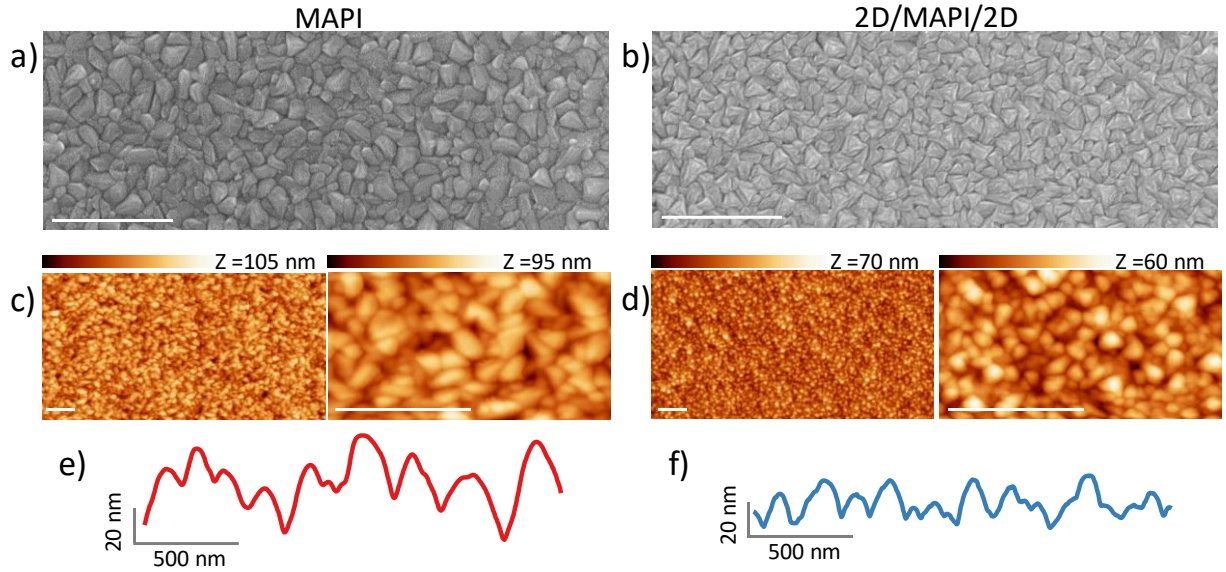

Figure 2. SEM pictures and AFM topographies at different magnifications of a,c) a MAPI film and of b,d) a 2D/MAPI/2D heterostructure. e,f) AFM profiles for the same samples. The scale bar in all SEM and AFM images is 1 μm.

In the 2D/MAPI/2D heterostructure (Figure 2b), we can already observe how the PEA_2PbI_4 affects the film growth and morphology, as the grain size is reduced and the surface seems more textured as compared to the bare MAPI.[6465] These effect correlates with the XRD diffraction discussed before (Figure S2). The sample surfaces were further analysed by atomic force microscopy (AFM). While homogeneous on a large scale (Figure 2c), the MAPI films surface was found to be rather rough, with a root mean square roughness R_{RMS} of 13 nm and average height z_{AVG} as high as 50 nm (Figure 2e and S4). The grain size reduction observed by SEM for the 2D/MAPI/2D heterostructure was also confirmed by AFM (Figure 2d), where the topography was characterized by a R_{RMS} = 8 nm and a strongly diminished z_{AVG} of 27 nm (Figure 2f). At the same time, the height distribution was found also to be narrower, indicating a more homogeneous

surface. Grain size reduction as a result of the interaction of a 3D perovskite with large cations has also been observed previously.[42,66]

To evaluate the potential of a 2D/MAPI/2D perovskite heterostructure in photovoltaics, we incorporated it in fully vacuum deposited perovskite solar cells using a p-i-n device layout (**Figure 3**a). The diodes were prepared on indium tin oxide (ITO), using molybdenum oxide (MoO_3, 5 nm) and N4,N4,N4″,N4″-tetra([1,1′-biphenyl]-4-yl)-[1,1′:4′,1″-terphenyl]-4,4″-diamine (TaTm, 10 nm) as the hole transport layer (HTL), a 500 nm thick MAPI films, fullerene (C60, 25 nm) and bathocuproine (BCP, 8 nm) as the electron transport layers (HTLs). The devices were completed with the deposition of a silver electrode (100 nm). The low dimensional PEA_2PbI_4 films were vacuum deposited in between the HTL/MAPI or the MAPI/ETL interfaces, varying the thickness between 2.5 and 10 nm. All layers were thermally deposited in high vacuum with a base pressure of 10^{-6} mbar. The current density-voltage (*J-V*) curves of PSCs were recorded under simulated AM 1.5G illumination (100 mW cm^{-2}, Figure 3), and the corresponding photovoltaic parameters are summarized in Table 1 (only for devices with 2.5 nm thick 2D films).

We initially fabricated and tested the triple layer heterojunctions of the type 2D/MAPI/2D. The heterojunction device with 2.5 nm thick 2D films showed a short circuit current density (J_{sc}) exceeding 20 mA/cm^{-2}, only slightly lower than the reference MAPI solar cell (Table 1 and Figure S5). While the open circuit voltage (V_{oc}) was found to decrease of only approximately 6-7 meV compared to the reference, we observed a strongly reduced FF (65.5%) even though the two 2D films are only 2.5 nm thick (Figure 3b). With increasing thickness of the low dimensional perovskite films, the FF further decreases to 49.7%, accompanied by a drastic reduction in the current density, being as low as 8 mA/cm^{-2} for 10 nm thick 2D films.

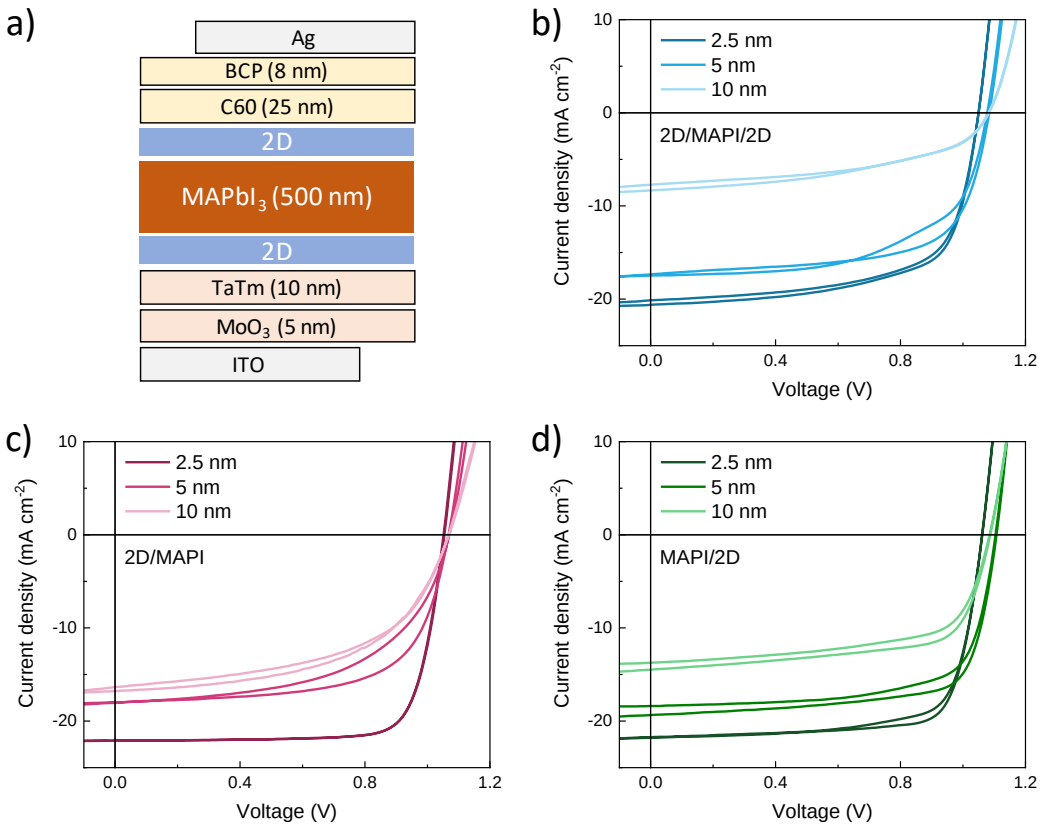

Figure 3. a) Schematics of the p-i-n solar cells employing a perovskite heterostructure as the active layer. *J–V* curve under 100 mW cm^{-2} illumination of the b) 2D/MAPI/2D, c) 2D/MAPI and d) MAPI/2D heterojunctions solar cells for different PEA_2PbI_4 layer thicknesses.

Clearly the 2D/MAPI/2D heterojunction solar cells suffer from hindered charge extraction, a situation that becomes more severe for thicker 2D films. This is in agreement with the formation of PEA_2PbI_4 films with insulating sheets perpendicular to the current flow, as described above. All solar cells based on the 2D/MAPI/2D heterostructure showed also hysteresis in the J-V curve when scanning in forward (from short to open circuit) or reverse (from open to short circuit) bias. However, the V_{oc} for the devices employing 5 and 10 nm thick PEA_2PbI_4 films was found to increase up to >1080 mV, meaning that the 2D films are indeed capable of reducing non-radiative recombination of the MAPI layer.

In order to rationalize the properties of the 2D/MAPI/2D heterostructure devices, we fabricated and characterized analogous solar cells based on either 2D/3D or 3D/2D bilayers as the active materials, with increasing thickness of the PEA_2PbI_4 films. The heterojunction device with the 2.5 nm thick 2D film at the front contact (2D/MAPI, Figure 3c), shows high short circuit current density (J_{sc}, 22.1 mA cm^{-2}) and very good rectification, with fill factor (FF) as high as 78.6% and negligible hysteresis. The V_{oc} is approximately

1.05 V, leading to a PCE of 18.3%, comparable to the reference MAPI solar cells. Increasing the thickness of PEA_2PbI_4 to 5 and 10 nm results in lower photocurrent (18 and 16.5 mA cm^{-2}, respectively) and causes again a drastic reduction of the FF, which is below 55% for both thicknesses. The cells with thicker 2D films show also hysteresis in the J-V curve. However, when compared to bare MAPI, the solar cell photovoltage is also found to increase to about 1070 mV for thicker 2D perovskite films.

Table 1. PV performance parameters extracted from the *J–V* characteristics of p-i-n solar cells of the control MAPI absorber device and of 2D/MAPI/2D, 2D/MAPI and MAPI/2D based PSCs with 2.5 nm thick PEA_2PbI_4 2D films.

Perovskite structure		V_{OC} [mV]	J_{SC} [mA cm^{-2}]	*FF* [%]	*PCE* [%]
MAPI	*fwd*	1057	22.7	77.2	18.6
	rev	1056	22.7	78.5	18.9
2D/MAPI/2D	*fwd*	1050	20.1	65.5	13.9
	rev	1050	20.6	66.0	14.3
2D/MAPI	*fwd*	1054	22.1	78.4	18.3
	rev	1051	22.1	78.6	18.3
MAPI/2D	*fwd*	1062	21.7	73.5	17.0
	rev	1061	21.8	76.6	17.7

A similar behaviour was observed for the solar cells based on the MAPI/2D heterojunction (Figure 3d), where the PEA_2PbI_4 is now deposited on top of MAPI, below the C60 ETL. The current density decreases with increasing thickness of the 2D perovskite films, from 21.8 mA cm^{-2} (2.5 nm) to approximately 14 mA cm^{-2} (10 nm). The J-V curves for devices including thicker (5 and 10 nm) 2D films show hysteresis, with slightly larger current densities (approximately 1 mA cm^{-2}) in reverse bias. Also for MAPI/2D heterojunctions the FF was observed to scale inversely with the thickness of PEA_2PbI_4, but not as drastically as in the case of 2D/MAPI structures. FF decreases from 73.5% to 63.9% when the 2D layer thickness is increased from 2.5 to 10 nm. Importantly, with this device configuration we do observe a substantial increase in the photovoltage, with the MAPI/2D solar cells having a V_{oc} exceeding 1.1 V for 5 nm thick PEA_2PbI_4 layers. This observation indicates that the 2D perovskite layer is indeed capable of reducing the non-radiative recombination within the MAPI film. Interestingly, the fact that no changes in photovoltage were observed with the 2D/MAPI heterojunction (as compared to bare MAPI), might indicate that the interface chemistry of the 2D/3D interface differs from that of the MAPI/2D one.

Figure 4 summarizes the thickness dependent photovoltage and FF measured on the different heterojunction solar cells. In general, we observe a trend where 2.5 nm thick films of PEA_2PbI_4,

independently on which side of the MAPI are deposited, do not lead to an appreciable increase in the photovoltage (for MAPI cells is 1055 mV), while they already undermine the charge extraction, as the FF diminishes (Figure 3b). One exception is the 2D/3D heterojunction, where the V_{oc} and FF are essentially unchanged with respect to the reference MAPI solar cells, leading to similar PCE exceeding 18%.

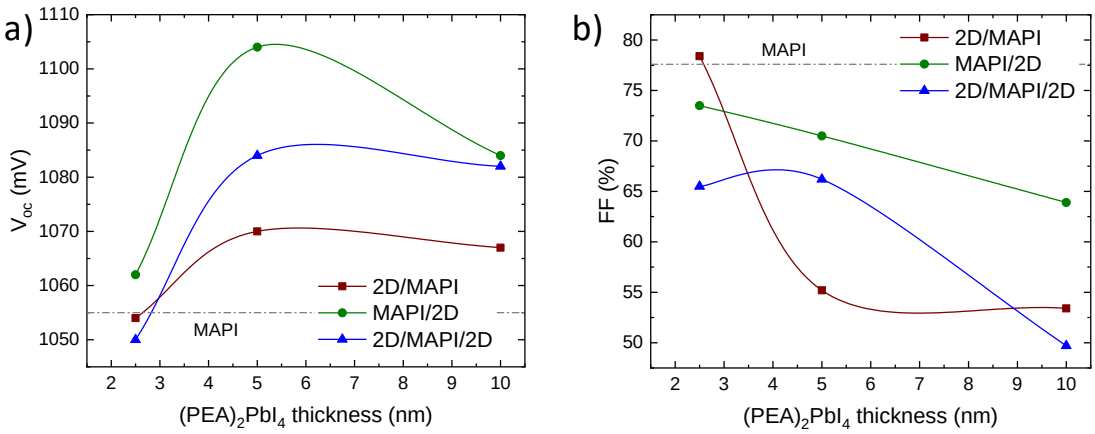

Figure 4. Trend of the a) V_{oc} and b) FF for the three different heterojunction solar cells as a function of the 2D perovskite (PEA_2PbI_4) layer thickness.

Increasing the 2D layer thickness to 5 nm leads to a general enhancement of the V_{oc}, with the devices based on the 2D/3D and 2D/3D/2D structures reaching 1070 and 1084 mV, respectively, and a peak for the 3D/2D heterojunctions solar cells at 1104 mV. While such 50 mV increase in V_{oc} might appear moderate, it corresponds to a 7-fold enhancement of the external photoluminescence quantum yield.[67,68] We note that devices with different thickness of the 2D films show comparable dark leakage current, indicating that the observed changes of voltage have no direct electrical origin (Figure S8). Hence the vacuum deposited PEA_2PbI_4 films on top of MAPI is indeed capable of reducing non-radiative charge recombination, although at the expense of FF (70%). For thicker (10 nm) 2D films, we observed a reduction of the V_{oc}, which is more prominent for the 3D/2D heterojunction with a 10 nm thick film. Although the incorporation of 2D perovskites at the interface with MAPI is beneficial in terms of photovoltage, it leads to a drop in FF which became more important once the PEA_2PbI_4 thickness increase from to 5 nm and 10 nm (Figure 3b). The loss in FF can be attributed to the unfavorable orientation of the insulating sheets formed by the bulky organic cations within the 2D perovskite films (Figure 1), perpendicularly oriented to the direction of the charge transport.

Beside the orientation of the 2D perovskite with respect to the substrate, another factor which can contribute to the loss in FF is the presence of an energy barrier for the charge extraction (either hole or electron, or both) at the 3D/2D heterojunction or at the perovskite/organic interfaces. Such energy barrier is related to a misalignment of the energy levels, which is likely to exist at least in one case (either 2D/3D or 3D/2D) as a consequence of the larger bandgap of PEA_2PbI_4 as compared to MAPI. The ionization energy (IE) can be used to estimate the valence band maximum (VBM) in an intrinsic semiconductor. We measured via air photoemission spectroscopy the IE of both 3D and 2D perovskites (Figure S6). We found an IE for MAPI of 5.0 eV, only slightly smaller as compared to recently reported ultraviolet photoemission spectroscopy measurements,[69] while a larger IE of 5.5 eV was measured for PEA_2PbI_4 films. This imply the presence of an energy barrier for the hole extraction of approximately 0.5 eV, which supports the sever drop in FF observed when PEA_2PbI_4 is deposited in between the HTL and the MAPI (Figure 3b). Estimating the bandgap of PEA_2PbI_4 from the absorption spectrum (2.4 eV) and considering a MAPI bandgap of 1.6 eV[69], the barrier for the electron extraction at the 3D/2D interface would be of 0.3 eV (Figure S6). The lower energy difference among the electronic affinities at the 3D/2D interface agrees with the smaller FF losses associated with using the 2D perovskite on top of the MAPI surface and below the ETL.

The vacuum deposited 2D/3D heterostructures were further studied by means of time resolved microwave conductivity (TRMC). **Figure 5**a depicts the normalized time-dependent conductance traces for bare MAPI and 2D/MAPI bilayers, obtained by selectively and homogeneously exciting the 3D MAPI film at 600 nm from both sides. Due to the lack of optical absorption at this wavelength, we did not observe any appreciable signal from the 2D layer. After a fast initial rise limited by the response time of the microwave cavity, the signals decay due to charge recombination or trapping. Interestingly, the decay kinetics of the MAPI and 2D/MAPI are very similar, and independent on the excitation side and the presence of the 2D layer. Hence, from this measurement, we cannot conclude that the MAPI film is effectively passivated by the 2D layer.

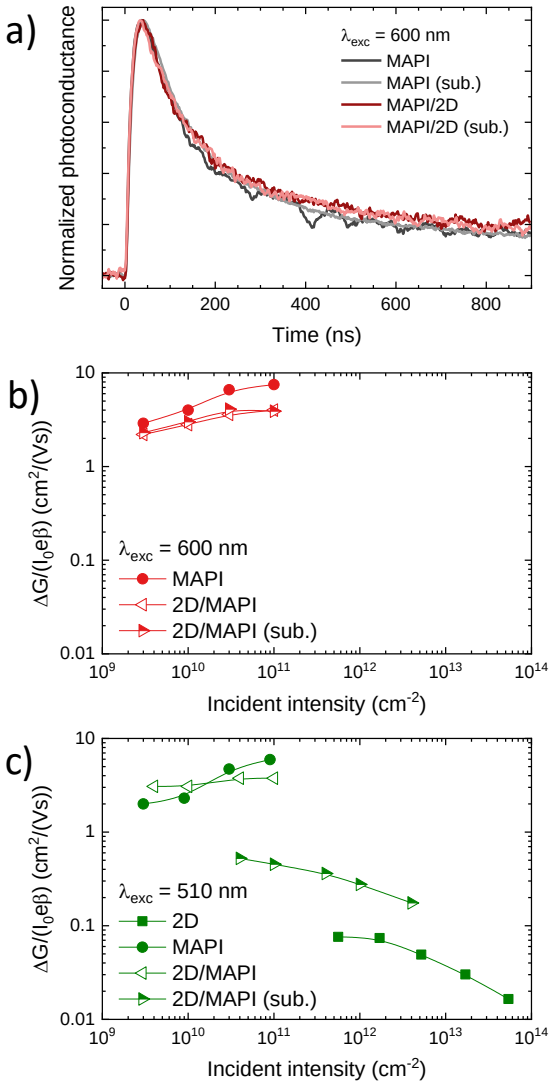

Figure 5 a) Normalised change in conductance for a MAPI film and a 2D/MAPI bilayer deposited on quartz, measured by TRMC with an incident laser pulse of 10^{11} photons/cm^2. Maximum TRMC signal heights expressed in charge carrier yield times mobility for excitation at b) 600 nm and c) 510 nm. The annotation (sub.) denotes that the light is shined through the quartz substrate.

From the maximum change in photoconductance, ΔG_{max}, the product of charge carrier generation efficiency per incident photon, η and the sum of electron and hole mobility, $\sum \mu$ is calculated using:

$$\eta \sum \mu = \frac{\Delta G_{max}}{I_0 e \beta} \qquad (1)$$

where I_0 is the incident intensity, e is the elementary charge and β is a geometrical factor. For both the 3D film as well as the 3D/2D bilayer the $\eta \sum \mu$ values are increasing slightly with light intensity reaching values close to 10 cm^2/Vs, which is comparable to values previously reported and discussed on evaporated 3D perovskite layers.[70,71] The slight difference in maximum mobility can be related to the different substrate on which the 3D MAPI layer has been deposited. Importantly, the dependence of the MAPI film with intensity is larger than that of the 2D/MAPI bilayers, which is almost constant (Figure 5b). Such dependence can be explained by the fact that the 3D film contains a substantial amount of deep traps, which become saturated at higher intensities.[72] This observation agrees with the higher V_{oc} values observed for the heterostructure devices (Figure 4a). Finally, we excited the samples at 510 nm, which corresponds with the maximum absorption of the excitonic band of the 2D perovskite (see Figure 5c). The 2D layer exhibits very low signal which can be explained by the high exciton binding energy preventing dissociation of the excitons into mobile carriers.[73] The MAPI films as well as the 3D/2D bilayer give signal intensities comparable to that of excitation at 600 nm implying the charge carrier yield is independent of the used wavelengths. Interestingly, exciting the 2D/MAPI sample through the 2D layer leads to a substantial decrease of the signal intensity. This can be explained by the fact that a substantial part of the incident light is absorbed by the 2D perovskite itself, and the excited states generated in the 2D layer do not lead to mobile carriers in the MAPI film by either charge or energy transfer. This inefficient charge carrier generation might partially explain the photocurrent losses observed in the heterostructure devices (Figure 3).

In summary, we show for the first time the fabrication of perovskite heterostructures by dual source vacuum deposition. This was achieved by vacuum processing thin layers of the 2D perovskite phenetylammonium lead iodide (PEA_2PbI_4) below and on top of a vacuum deposited methylammonium lead iodide (MAPI) film. We investigated the morphology, structure and optical properties of the 2D and 3D separately, as well as of the 2D/3D/2D heterostructure, and observed that vacuum deposited PEA_2PbI_4 films tend to grow with the alternating inorganic and organic sheets parallel to the substrate. For this reason, when incorporated into devices, the 2D/3D/2D perovskite heterostructure shows a strongly hindered charge extraction, result of an interplay of parameters among which the preferential in-plane orientation of the 2D film, the low carrier mobility, and the mismatch in the transport energy levels. By separately studying the 2D/3D and 3D/2D bilayers, we identify a trade-off between the solar cells photovoltage and fill factor, with 3D/2D heterojunction solar cells having open-circuit voltage as high as 1.1 V. By time resolved microwave conductivity we observed that the density of deep traps in the MAPI active layers is reduced in the presence of the 2D perovskite, however, the latter leads to a reduced photocurrent as we did not observe any charge- or energy transfer from the 2D film to the MAPI. In general, our results show a marked difference between vacuum –deposited and solution-processed 3D/2D architecture, with unfavorable orientation but high phase purity obtained by dual-source vapor deposition. Future work will address the vacuum deposition of

vertically oriented 2D perovskite films, in order to promote charge transport, and will focus on their role on the overall device stability.

Acknowledgements

The research leading to these results has received funding from the European Union Programme for Research and Innovation Horizon 2020 (2014–2020) under the Marie Skłodowska-Curie Grant Agreement PerovSAMs No. 747599 and the Spanish Ministry of Economy and Competitiveness (MINECO) via the Unidad de Excelencia María de Maeztu MDM-2015-0538, MAT2017-88821-R, PCIN-2015-255, PCIN-2017-014, and the Generalitat Valenciana (Prometeo/2016/135). M.S. acknowledges the MINECO for his RyC contracts. D.G acknowledges the funding from the China Scholarship Council (CSC).

Supporting Information Available: Experimental methods, XRD patterns of PEA_2PbI_4 measured as prepared and after 6 months, XRD patterns of 3D perovskite and (2D/3D/2D) heterostructure, absorption spectra and roughness analysis of 3D perovskite and (2D/3D/2D) perovskite heterostructure, J-V curves of the reference 3D MAPI solar cell and of 2D/3D, 3D/2D and 2D/3D/2D heterojunctions devices with 2.5 nm PEA_2PbI_4, APS of 3D and 2D thin film and flat band energy diagram with ionization energies and electron affinity.

References

(1) Li, W.; Wang, Z.; Deschler, F.; Gao, S.; Friend, R. H.; Cheetham, A. K. Chemically Diverse and Multifunctional Hybrid Organic–Inorganic Perovskites. *Nat. Rev. Mater.* **2017**, *2* (3), 16099. https://doi.org/10.1038/natrevmats.2016.99.

(2) Huang, J.; Yuan, Y.; Shao, Y.; Yan, Y. Understanding the Physical Properties of Hybrid Perovskites for Photovoltaic Applications. *Nat. Rev. Mater.* **2017**, *2* (7), 17042. https://doi.org/10.1038/natrevmats.2017.42.

(3) Brenner, T. M.; Egger, D. A.; Kronik, L.; Hodes, G.; Cahen, D. Hybrid Organic—Inorganic Perovskites: Low-Cost Semiconductors with Intriguing Charge-Transport Properties. *Nat. Rev. Mater.* **2016**, *1* (1), 15007. https://doi.org/10.1038/natrevmats.2015.7.

(4) Swartwout, R.; Hoerantner, M. T.; Bulović, V. Scalable Deposition Methods for Large-Area Production of Perovskite Thin Films. *Energy Environ. Mater.* **2019**, *2* (2), 119–143. https://doi.org/10.1002/eem2.12043.

(5) Li, Z.; Klein, T. R.; Kim, D. H.; Yang, M.; Berry, J. J.; van Hest, M. F. A. M.; Zhu, K. Scalable Fabrication of Perovskite Solar Cells. *Nat. Rev. Mater.* **2018**, *3* (4), 18017. https://doi.org/10.1038/natrevmats.2018.17.

(6) Green, M. A.; Dunlop, E. D.; Levi, D. H.; Hohl-Ebinger, J.; Yoshita, M.; Ho-Baillie, A. W. Y. Solar Cell Efficiency Tables (Version 54). *Prog. Photovoltaics Res. Appl.* **2019**, *27* (7), 565–575. https://doi.org/10.1002/pip.3171.

(7) Saliba, M. Polyelemental, Multicomponent Perovskite Semiconductor Libraries through Combinatorial Screening. *Adv. Energy Mater.* **2019**, *9* (25), 1803754. https://doi.org/10.1002/aenm.201803754.

(8) Zhao, Y.; Zhu, K. Organic–Inorganic Hybrid Lead Halide Perovskites for Optoelectronic and Electronic Applications. *Chem. Soc. Rev.* **2016**, *45* (3), 655–689. https://doi.org/10.1039/C4CS00458B.
(9) Stoumpos, C. C.; Kanatzidis, M. G. Halide Perovskites: Poor Man's High-Performance Semiconductors. *Adv. Mater.* **2016**, *28* (28), 5778–5793. https://doi.org/10.1002/adma.201600265.
(10) Zhao, D.; Yu, Y.; Wang, C.; Liao, W.; Shrestha, N.; Grice, C. R.; Cimaroli, A. J.; Guan, L.; Ellingson, R. J.; Zhu, K.; et al. Low-Bandgap Mixed Tin–Lead Iodide Perovskite Absorbers with Long Carrier Lifetimes for All-Perovskite Tandem Solar Cells. *Nat. Energy* **2017**, *2* (4), 17018. https://doi.org/10.1038/nenergy.2017.18.
(11) Wang, J.; Fu, W.; Jariwala, S.; Sinha, I.; K-Y Jen, A.; Ginger, D. S. Reducing Surface Recombination Velocities at the Electrical Contacts Will Improve Perovskite Photovoltaics. **2019**, *8*, 31. https://doi.org/10.1021/acsenergylett.8b02058.
(12) Ball, J. M.; Petrozza, A. Defects in Perovskite-Halides and Their Effects in Solar Cells. *Nat. Energy* **2016**, *1* (11), 16149. https://doi.org/10.1038/nenergy.2016.149.
(13) Aydin, E.; Bastiani, M.; Wolf, S. Defect and Contact Passivation for Perovskite Solar Cells. *Adv. Mater.* **2019**, 1900428. https://doi.org/10.1002/adma.201900428.
(14) Wang, L.; McCleese, C.; Kovalsky, A.; Zhao, Y.; Burda, C. Femtosecond Time-Resolved Transient Absorption Spectroscopy of $CH_3NH_3PbI_3$ Perovskite Films: Evidence for Passivation Effect of PbI_2. *J. Am. Chem. Soc.* **2014**, *136* (35), 12205–12208. https://doi.org/10.1021/ja504632z.
(15) Chen, Q.; Zhou, H.; Song, T.-B.; Luo, S.; Hong, Z.; Duan, H.-S.; Dou, L.; Liu, Y.; Yang, Y. Controllable Self-Induced Passivation of Hybrid Lead Iodide Perovskites toward High Performance Solar Cells. *Nano Lett.* **2014**, *14* (7), 4158–4163. https://doi.org/10.1021/nl501838y.
(16) Qiu, W.; Merckx, T.; Jaysankar, M.; Masse de la Huerta, C.; Rakocevic, L.; Zhang, W.; Paetzold, U. W.; Gehlhaar, R.; Froyen, L.; Poortmans, J.; et al. Pinhole-Free Perovskite Films for Efficient Solar Modules. *Energy Environ. Sci.* **2016**, *9* (2), 484–489. https://doi.org/10.1039/C5EE03703D.
(17) Li, N.; Tao, S.; Chen, Y.; Niu, X.; Onwudinanti, C. K.; Hu, C.; Qiu, Z.; Xu, Z.; Zheng, G.; Wang, L.; et al. Cation and Anion Immobilization through Chemical Bonding Enhancement with Fluorides for Stable Halide Perovskite Solar Cells. *Nat. Energy* **2019**, *4* (5), 408–415. https://doi.org/10.1038/s41560-019-0382-6.
(18) Abdi-Jalebi, M.; Andaji-Garmaroudi, Z.; Cacovich, S.; Stavrakas, C.; Philippe, B.; Richter, J. M.; Alsari, M.; Booker, E. P.; Hutter, E. M.; Pearson, A. J.; et al. Maximizing and Stabilizing Luminescence from Halide Perovskites with Potassium Passivation. *Nature* **2018**, *555* (7697), 497–501. https://doi.org/10.1038/nature25989.
(19) Saliba, M.; Matsui, T.; Domanski, K.; Seo, J.-Y.; Ummadisingu, A.; Zakeeruddin, S. M.; Correa-Baena, J.-P.; Tress, W. R.; Abate, A.; Hagfeldt, A.; et al. Incorporation of Rubidium Cations into Perovskite Solar Cells Improves Photovoltaic Performance. *Science (80-.).* **2016**, *354* (6309), 206–209. https://doi.org/10.1126/science.aah5557.
(20) Wang, Q.; Dong, Q.; Li, T.; Gruverman, A.; Huang, J. Thin Insulating Tunneling Contacts for Efficient and Water-Resistant Perovskite Solar Cells. *Adv. Mater.* **2016**, *28* (31), 6734–6739. https://doi.org/10.1002/adma.201600969.
(21) Liang, P.-W.; Chueh, C.-C.; Williams, S. T.; Jen, A. K.-Y. Roles of Fullerene-Based Interlayers in Enhancing the Performance of Organometal Perovskite Thin-Film Solar Cells. *Adv. Energy Mater.* **2015**, *5* (10), 1402321. https://doi.org/10.1002/aenm.201402321.
(22) Shao, Y.; Xiao, Z.; Bi, C.; Yuan, Y.; Huang, J. Origin and Elimination of Photocurrent Hysteresis by Fullerene Passivation in CH3NH3PbI3 Planar Heterojunction Solar Cells. *Nat. Commun.* **2014**, *5* (1), 5784. https://doi.org/10.1038/ncomms6784.
(23) Wang, K.; Neophytou, M.; Aydin, E.; Wang, M.; Laurent, T.; Harrison, G. T.; Liu, J.; Liu, W.; De Bastiani, M.; Khan, J. I.; et al. Triarylphosphine Oxide as Cathode Interfacial Material for Inverted Perovskite Solar Cells. *Adv. Mater. Interfaces* **2019**, 1900434. https://doi.org/10.1002/admi.201900434.

(24) Zhao, T.; Chueh, C.-C.; Chen, Q.; Rajagopal, A.; Jen, A. K.-Y. Defect Passivation of Organic–Inorganic Hybrid Perovskites by Diammonium Iodide toward High-Performance Photovoltaic Devices. *ACS Energy Lett.* **2016**, *1* (4), 757–763. https://doi.org/10.1021/acsenergylett.6b00327.
(25) Zheng, X.; Chen, B.; Dai, J.; Fang, Y.; Bai, Y.; Lin, Y.; Wei, H.; Zeng, X. C.; Huang, J. Defect Passivation in Hybrid Perovskite Solar Cells Using Quaternary Ammonium Halide Anions and Cations. *Nat. Energy* **2017**, *2* (7), 17102. https://doi.org/10.1038/nenergy.2017.102.
(26) Stoumpos, C. C.; Soe, C. M. M.; Tsai, H.; Nie, W.; Blancon, J.-C.; Cao, D. H.; Liu, F.; Traoré, B.; Katan, C.; Even, J.; et al. High Members of the 2D Ruddlesden-Popper Halide Perovskites: Synthesis, Optical Properties, and Solar Cells of (CH 3 (CH 2) 3 NH 3) 2 (CH 3 NH 3) 4 Pb 5 I 16. *Chem* **2017**, *2* (3), 427–440. https://doi.org/10.1016/j.chempr.2017.02.004.
(27) Yusoff, A. R. bin M.; Nazeeruddin, M. K. Low-Dimensional Perovskites: From Synthesis to Stability in Perovskite Solar Cells. *Adv. Energy Mater.* **2018**, *8* (26), 1702073. https://doi.org/10.1002/aenm.201702073.
(28) Thrithamarassery Gangadharan, D.; Ma, D. Searching for Stability at Lower Dimensions: Current Trends and Future Prospects of Layered Perovskite Solar Cells. *Energy Environ. Sci.* **2019**, 10.1039/C9EE01591D. https://doi.org/10.1039/C9EE01591D.
(29) Quan, L. N.; Yuan, M.; Comin, R.; Voznyy, O.; Beauregard, E. M.; Hoogland, S.; Buin, A.; Kirmani, A. R.; Zhao, K.; Amassian, A.; et al. Ligand-Stabilized Reduced-Dimensionality Perovskites. *J. Am. Chem. Soc.* **2016**, *138* (8), 2649–2655. https://doi.org/10.1021/jacs.5b11740.
(30) Milot, R. L.; Sutton, R. J.; Eperon, G. E.; Haghighirad, A. A.; Martinez Hardigree, J.; Miranda, L.; Snaith, H. J.; Johnston, M. B.; Herz, L. M. Charge-Carrier Dynamics in 2D Hybrid Metal–Halide Perovskites. *Nano Lett.* **2016**, *16* (11), 7001–7007. https://doi.org/10.1021/acs.nanolett.6b03114.
(31) Cohen, B.-E.; Wierzbowska, M.; Etgar, L. High Efficiency and High Open Circuit Voltage in Quasi 2D Perovskite Based Solar Cells. *Adv. Funct. Mater.* **2017**, *27* (5), 1604733. https://doi.org/10.1002/adfm.201604733.
(32) Mitzi, D. B. Solution-Processed Inorganic Semiconductors. *J. Mater. Chem.* **2004**, *14* (15), 2355. https://doi.org/10.1039/b403482a.
(33) Cao, D. H.; Stoumpos, C. C.; Farha, O. K.; Hupp, J. T.; Kanatzidis, M. G. 2D Homologous Perovskites as Light-Absorbing Materials for Solar Cell Applications. *J. Am. Chem. Soc.* **2015**, *137* (24), 7843–7850. https://doi.org/10.1021/jacs.5b03796.
(34) Koh, T. M.; Shanmugam, V.; Schlipf, J.; Oesinghaus, L.; Müller-Buschbaum, P.; Ramakrishnan, N.; Swamy, V.; Mathews, N.; Boix, P. P.; Mhaisalkar, S. G. Nanostructuring Mixed-Dimensional Perovskites: A Route Toward Tunable, Efficient Photovoltaics. *Adv. Mater.* **2016**, *28* (19), 3653–3661. https://doi.org/10.1002/adma.201506141.
(35) Chen, Y.; Sun, Y.; Peng, J.; Zhang, W.; Su, X.; Zheng, K.; Pullerits, T.; Liang, Z. Tailoring Organic Cation of 2D Air-Stable Organometal Halide Perovskites for Highly Efficient Planar Solar Cells. *Adv. Energy Mater.* **2017**, *7* (18), 1700162. https://doi.org/10.1002/aenm.201700162.
(36) Ma, C.; Shen, D.; Ng, T.-W.; Lo, M.-F.; Lee, C.-S. 2D Perovskites with Short Interlayer Distance for High-Performance Solar Cell Application. *Adv. Mater.* **2018**, *30* (22), 1800710. https://doi.org/10.1002/adma.201800710.
(37) Jiang, W.; Ying, J.; Zhou, W.; Shen, K.; Liu, X.; Gao, X.; Guo, F.; Gao, Y.; Yang, T. A New Layered Nano Hybrid Perovskite Film with Enhanced Resistance to Moisture-Induced Degradation. *Chem. Phys. Lett.* **2016**, *658*, 71–75. https://doi.org/10.1016/J.CPLETT.2016.05.054.
(38) Yantara, N.; Bruno, A.; Iqbal, A.; Jamaludin, N. F.; Soci, C.; Mhaisalkar, S.; Mathews, N. Designing Efficient Energy Funneling Kinetics in Ruddlesden–Popper Perovskites for High-Performance Light-Emitting Diodes. *Adv. Mater.* **2018**, *30* (33), 1800818. https://doi.org/10.1002/adma.201800818.
(39) Yuan, M.; Quan, L. N.; Comin, R.; Walters, G.; Sabatini, R.; Voznyy, O.; Hoogland, S.; Zhao, Y.; Beauregard, E. M.; Kanjanaboos, P.; et al. Perovskite Energy Funnels for Efficient Light-Emitting Diodes. *Nat. Nanotechnol.* **2016**, *11*, 872. https://doi.org/10.1038/nnano.2016.110.
(40) Gharibzadeh, S.; Abdollahi Nejand, B.; Jakoby, M.; Abzieher, T.; Hauschild, D.;

Moghadamzadeh, S.; Schwenzer, J. A.; Brenner, P.; Schmager, R.; Haghighirad, A. A.; et al. Record Open-Circuit Voltage Wide-Bandgap Perovskite Solar Cells Utilizing 2D/3D Perovskite Heterostructure. *Adv. Energy Mater.* **2019**, *9* (21), 1803699. https://doi.org/10.1002/aenm.201803699.

(41) Grancini, G.; Nazeeruddin, M. K. Dimensional Tailoring of Hybrid Perovskites for Photovoltaics. *Nat. Rev. Mater.* **2019**, *4* (1), 4–22. https://doi.org/10.1038/s41578-018-0065-0.

(42) Wang, Z.; Lin, Q.; Chmiel, F. P.; Sakai, N.; Herz, L. M.; Snaith, H. J. Efficient Ambient-Air-Stable Solar Cells with 2D–3D Heterostructured Butylammonium-Caesium-Formamidinium Lead Halide Perovskites. *Nat. Energy* **2017**, *2* (9), 17135. https://doi.org/10.1038/nenergy.2017.135.

(43) Poli, I.; Eslava, S.; Cameron, P. Tetrabutylammonium Cations for Moisture-Resistant and Semitransparent Perovskite Solar Cells. *J. Mater. Chem. A* **2017**, *5* (42), 22325–22333. https://doi.org/10.1039/C7TA06735F.

(44) Liu, Y.; Akin, S.; Pan, L.; Uchida, R.; Arora, N.; Milić, J. V; Hinderhofer, A.; Schreiber, F.; Uhl, A. R.; Zakeeruddin, S. M.; et al. Ultrahydrophobic 3D/2D Fluoroarene Bilayer-Based Water-Resistant Perovskite Solar Cells with Efficiencies Exceeding 22. *Sci. Adv.* **2019**, *5* (6), eaaw2543. https://doi.org/10.1126/sciadv.aaw2543.

(45) Ye, T.; Bruno, A.; Han, G.; Koh, T. M.; Li, J.; Jamaludin, N. F.; Soci, C.; Mhaisalkar, S. G.; Leong, W. L. Efficient and Ambient-Air-Stable Solar Cell with Highly Oriented 2D@3D Perovskites. *Adv. Funct. Mater.* **2018**, *28* (30), 1801654. https://doi.org/10.1002/adfm.201801654.

(46) Kim, J.; Ho-Baillie, A.; Huang, S. Review of Novel Passivation Techniques for Efficient and Stable Perovskite Solar Cells. *Sol. RRL* **2019**, *3* (4), 1800302. https://doi.org/10.1002/solr.201800302.

(47) Lee, D. S.; Yun, J. S.; Kim, J.; Soufiani, A. M.; Chen, S.; Cho, Y.; Deng, X.; Seidel, J.; Lim, S.; Huang, S.; et al. Passivation of Grain Boundaries by Phenethylammonium in Formamidinium-Methylammonium Lead Halide Perovskite Solar Cells. *ACS Energy Lett.* **2018**, *3* (3), 647–654. https://doi.org/10.1021/acsenergylett.8b00121.

(48) Cho, Y.; Soufiani, A. M.; Yun, J. S.; Kim, J.; Lee, D. S.; Seidel, J.; Deng, X.; Green, M. A.; Huang, S.; Ho-Baillie, A. W. Y. Mixed 3D-2D Passivation Treatment for Mixed-Cation Lead Mixed-Halide Perovskite Solar Cells for Higher Efficiency and Better Stability. *Adv. Energy Mater.* **2018**, *8* (20), 1703392. https://doi.org/10.1002/aenm.201703392.

(49) Cho, K. T.; Grancini, G.; Lee, Y.; Oveisi, E.; Ryu, J.; Almora, O.; Tschumi, M.; Schouwink, P. A.; Seo, G.; Heo, S.; et al. Selective Growth of Layered Perovskites for Stable and Efficient Photovoltaics. *Energy Environ. Sci.* **2018**, *11* (4), 952–959. https://doi.org/10.1039/C7EE03513F.

(50) Grancini, G.; Roldán-Carmona, C.; Zimmermann, I.; Mosconi, E.; Lee, X.; Martineau, D.; Narbey, S.; Oswald, F.; De Angelis, F.; Graetzel, M.; et al. One-Year Stable Perovskite Solar Cells by 2D/3D Interface Engineering. *Nat. Commun.* **2017**, *8* (1), 15684. https://doi.org/10.1038/ncomms15684.

(51) Cho, K. T.; Zhang, Y.; Orlandi, S.; Cavazzini, M.; Zimmermann, I.; Lesch, A.; Tabet, N.; Pozzi, G.; Grancini, G.; Nazeeruddin, M. K. Water-Repellent Low-Dimensional Fluorous Perovskite as Interfacial Coating for 20% Efficient Solar Cells. *Nano Lett.* **2018**, *18* (9), 5467–5474. https://doi.org/10.1021/acs.nanolett.8b01863.

(52) Quintero-Bermudez, R.; Gold-Parker, A.; Proppe, A. H.; Munir, R.; Yang, Z.; Kelley, S. O.; Amassian, A.; Toney, M. F.; Sargent, E. H. Compositional and Orientational Control in Metal Halide Perovskites of Reduced Dimensionality. *Nat. Mater.* **2018**, *17* (10), 900–907. https://doi.org/10.1038/s41563-018-0154-x.

(53) Ávila, J.; Momblona, C.; Boix, P. P.; Sessolo, M.; Bolink, H. J. Vapor-Deposited Perovskites: The Route to High-Performance Solar Cell Production? *Joule* **2017**, *1* (3), 431–442. https://doi.org/10.1016/j.joule.2017.07.014.

(54) Forgács, D.; Gil-Escrig, L.; Pérez-Del-Rey, D.; Momblona, C.; Werner, J.; Niesen, B.; Ballif, C.; Sessolo, M.; Bolink, H. J. Efficient Monolithic Perovskite/Perovskite Tandem Solar Cells. *Adv. Energy Mater.* **2016**, 1602121. https://doi.org/10.1002/aenm.201602121.

(55) Ávila, J.; Momblona, C.; Boix, P.; Sessolo, M.; Anaya, M.; Lozano, G.; Vandewal, K.; Míguez, H.; Bolink, H. J. High Voltage Vacuum-Deposited $CH_3NH_3PbI_3$–$CH_3NH_3PbI_3$ Tandem Solar Cells. *Energy Environ. Sci.* **2018**, *11* (11), 3292–3297. https://doi.org/10.1039/C8EE01936C.
(56) Borchert, J.; Milot, R. L.; Patel, J. B.; Davies, C. L.; Wright, A. D.; Martínez Maestro, L.; Snaith, H. J.; Herz, L. M.; Johnston, M. B. Large-Area, Highly Uniform Evaporated Formamidinium Lead Triiodide Thin Films for Solar Cells. *ACS Energy Lett.* **2017**, *2* (12), 2799–2804. https://doi.org/10.1021/acsenergylett.7b00967.
(57) Fan, P.; Gu, D.; Liang, G.-X.; Luo, J.-T.; Chen, J.-L.; Zheng, Z.-H.; Zhang, D.-P. High-Performance Perovskite CH3NH3PbI3 Thin Films for Solar Cells Prepared by Single-Source Physical Vapour Deposition. *Sci. Rep.* **2016**, *6* (1), 29910. https://doi.org/10.1038/srep29910.
(58) Lin, D.; Zhang, T.; Wang, J.; Long, M.; Xie, F.; Chen, J.; Wu, B.; Shi, T.; Yan, K.; Xie, W.; et al. Stable and Scalable 3D-2D Planar Heterojunction Perovskite Solar Cells via Vapor Deposition. *Nano Energy* **2019**, *59*, 619–625. https://doi.org/10.1016/j.nanoen.2019.03.014.
(59) Silver, S.; Yin, J.; Li, H.; Brédas, J.-L.; Kahn, A. Characterization of the Valence and Conduction Band Levels of $n = 1$ 2D Perovskites: A Combined Experimental and Theoretical Investigation. *Adv. Energy Mater.* **2018**, *8* (16), 1703468. https://doi.org/10.1002/aenm.201703468.
(60) Roldán-Carmona, C.; Gratia, P.; Zimmermann, I.; Grancini, G.; Gao, P.; Graetzel, M.; Nazeeruddin, M. K. High Efficiency Methylammonium Lead Triiodide Perovskite Solar Cells: The Relevance of Non-Stoichiometric Precursors. *Energy Environ. Sci.* **2015**, *8* (12), 3550–3556. https://doi.org/10.1039/C5EE02555A.
(61) Liu, M.; Johnston, M. B.; Snaith, H. J. Efficient Planar Heterojunction Perovskite Solar Cells by Vapour Deposition. *Nature* **2013**, *501* (7467), 395–398. https://doi.org/10.1038/nature12509.
(62) Huang, X.; Sendner, M.; Müller, C.; Sessolo, M.; Gil-Escrig, L.; Kowalsky, W.; Pucci, A.; Beck, S.; Lovrinčić, R. Quantifying the Composition of Methylammonium Lead Iodide Perovskite Thin Films with Infrared Spectroscopy. *J. Phys. Chem. C* **2019**, *123* (36), 22083–22088. https://doi.org/10.1021/acs.jpcc.9b07194.
(63) Palazon, F.; Pérez-del-Rey, D.; Dänekamp, B.; Dreessen, C.; Sessolo, M.; Boix, P. P.; Bolink, H. J. Room-Temperature Cubic Phase Crystallization and High Stability of Vacuum-Deposited Methylammonium Lead Triiodide Thin Films for High-Efficiency Solar Cells. *Adv. Mater.* **2019**, *31* (39), 1902692. https://doi.org/10.1002/adma.201902692.
(64) Olthof, S.; Meerholz, K. Substrate-Dependent Electronic Structure and Film Formation of MAPbI3 Perovskites. *Sci. Rep.* **2017**, *7*, 40267.
(65) Parrott, E. S.; Patel, J. B.; Haghighirad, A.-A.; Snaith, H. J.; Johnston, M. B.; Herz, L. M. Growth Modes and Quantum Confinement in Ultrathin Vapour-Deposited MAPbI3 Films. *Nanoscale* **2019**, *11* (30), 14276–14284. https://doi.org/10.1039/C9NR04104D.
(66) Lu, J.; Jiang, L.; Li, W.; Li, F.; Pai, N. K.; Scully, A. D.; Tsai, C.-M.; Bach, U.; Simonov, A. N.; Cheng, Y.-B.; et al. Diammonium and Monoammonium Mixed-Organic-Cation Perovskites for High Performance Solar Cells with Improved Stability. *Adv. Energy Mater.* **2017**, *7* (18), 1700444. https://doi.org/10.1002/aenm.201700444.
(67) Braly, I. L.; deQuilettes, D. W.; Pazos-Outón, L. M.; Burke, S.; Ziffer, M. E.; Ginger, D. S.; Hillhouse, H. W. Hybrid Perovskite Films Approaching the Radiative Limit with over 90% Photoluminescence Quantum Efficiency. *Nat. Photonics* **2018**, *12* (6), 355–361. https://doi.org/10.1038/s41566-018-0154-z.
(68) Ross, R. T. Some Thermodynamics of Photochemical Systems. *J. Chem. Phys.* **1967**, *46* (12), 4590–4593. https://doi.org/10.1063/1.1840606.
(69) Endres, J.; Egger, D. A.; Kulbak, M.; Kerner, R. A.; Zhao, L.; Silver, S. H.; Hodes, G.; Rand, B. P.; Cahen, D.; Kronik, L.; et al. Valence and Conduction Band Densities of States of Metal Halide Perovskites: A Combined Experimental–Theoretical Study. *J. Phys. Chem. Lett.* **2016**, *7* (14), 2722–2729. https://doi.org/10.1021/acs.jpclett.6b00946.
(70) Momblona, C.; Gil-Escrig, L.; Bandiello, E.; Hutter, E. M.; Sessolo, M.; Lederer, K.; Blochwitz-

Nimoth, J.; Bolink, H. J. Efficient Vacuum Deposited P-i-n and n-i-p Perovskite Solar Cells Employing Doped Charge Transport Layers. *Energy Environ. Sci.* **2016**, *9* (11), 3456–3463. https://doi.org/10.1039/C6EE02100J.

(71) Hutter, E. M.; Hofman, J.-J.; Petrus, M. L.; Moes, M.; Abellón, R. D.; Docampo, P.; Savenije, T. J. Charge Transfer from Methylammonium Lead Iodide Perovskite to Organic Transport Materials: Efficiencies, Transfer Rates, and Interfacial Recombination. *Adv. Energy Mater.* **2017**, *7* (13), 1602349. https://doi.org/10.1002/aenm.201602349.

(72) Savenije, T. J.; Huijser, A.; Vermeulen, M. J. W.; Katoh, R. Charge Carrier Dynamics in TiO2 Nanoparticles at Various Temperatures. *Chem. Phys. Lett.* **2008**, *461* (1–3), 93–96. https://doi.org/10.1016/j.cplett.2008.06.078.

(73) Gélvez-Rueda, M. C.; Hutter, E. M.; Cao, D. H.; Renaud, N.; Stoumpos, C. C.; Hupp, J. T.; Savenije, T. J.; Kanatzidis, M. G.; Grozema, F. C. Interconversion between Free Charges and Bound Excitons in 2D Hybrid Lead Halide Perovskites. *J. Phys. Chem. C* **2017**, *121* (47), 26566–26574. https://doi.org/10.1021/acs.jpcc.7b10705.